Chemical Science

ROYAL SOCIETY OF CHEMISTRY

EDGE ARTICLE

Cite this: *Chem. Sci.*, 2023, **14**, 8842

All publication charges for this article have been paid for by the Royal Society of Chemistry

Controlling NIR-II emitting gold organic/inorganic nanohybrids with tunable morphology and surface PEG density for dynamic visualization of vascular dysfunction†

Tingyao Zhou,‡[ab] Menglei Zha,‡[a] Hao Tang,[a] Kai Li [a] and Xingyu Jiang *[a]

Received 5th May 2023
Accepted 16th July 2023

DOI: 10.1039/d3sc02290k

rsc.li/chemical-science

Luminescent Au nanoparticles (AuNPs) and their organic/inorganic nanohybrids are of interest due to their favorable properties and promising biomedical applications. However, most existing AuNP-based hybrid nanostructures cannot satisfy high efficiency in synthesis, deep tissue penetration, and long blood circulation simultaneously, thus cannot be employed in dynamic monitoring of biomedical applications. In this paper, using Pluronic F127 as a template, we report a robust approach for one-pot synthesis of AuNP-based organic/inorganic nanohybrids (AuNHs) with bright luminescence in the second near-infrared (NIR-II) window, tunable shape, and controllable surface polyethylene glycol (PEG) density. The nanohybrids could be controlled from a necklace-like shape with a dense brush PEG configuration to a spherical structure with a brush PEG coating, which greatly impacts the *in vivo* biological behavior. Compared to spherical AuNHs, the necklace-shaped AuNHs present a higher quantum yield and longer blood circulation, which are superior to most of the individual AuNPs. With these outstanding features, the necklace-shaped AuNHs could achieve real-time, dynamic visualization of vascular dysfunction, capable of directing the precise administration of thrombolytics (a medicine for the breakdown of blood clots). These findings could provide a powerful guide for designing novel NIR-II nanoprobes toward *in vivo* dynamic information visualization.

Introduction

Vascular dysfunctions are closely related to the progress of various life-threatening diseases, including cancer, stroke, and myocardial infarction. Examining vascular anomalies is crucial for early diagnosis and guided therapy of these related diseases.[1–3] Currently, computed tomography (CT), ultrasound (US), and magnetic resonance imaging (MRI) are the conventional non-invasive imaging modalities in a clinic for the detection of vascular anomalies.[4,5] Nevertheless, most of them only afford delayed visualization with a low spatial resolution. In addition, some show ionizing radiation risks or suffer from operator dependence and artifacts. Optical imaging in the second near-infrared (NIR-II) window (1000–1700 nm) has gained considerable attention for vascular dysfunction imaging due to the rapid feedback, effective cost, high resolution, deep tissue penetration, and the absence of ionizing radiation.[6–8] In the past decades, these features have promoted frequent emergence and fast development of a series of NIR-II fluorophores, such as single-walled carbon nanotubes,[9] quantum dots,[10,11] organic dyes,[12–15] rare earth nanoparticles (NPs),[16,17] and semiconductor polymer dots,[18] for the observation of vascular dysfunction. Despite such progress, much work is still needed to advance NIR-II fluorophores with high synthetic efficiency, good safety, and long blood circulation to achieve dynamic monitoring of vascular dysfunctions.

Luminescent AuNPs are considered promising candidates for *in vivo* imaging because of inherent features, including ultrasmall size ($d < 3$ nm), low toxicity, good photostability, and ease of preparation.[19–23] NIR-II luminescence allows deep tissue penetration of ultrasmall AuNPs with high resolution, largely expanding their biological applications to *in vivo* biosensing, blood vessel, bone, and gastrointestinal imaging.[24–28] Previous efforts were devoted to preparing individual NIR-II-emitting AuNPs protected by thiolate, alkynyl, or phosphine groups.[29–32] However, the individual ultrasmall AuNPs usually show low quantum yield (QY) in the NIR-II region and possess short retention half-life time in the blood (2–25.8 min), unfavourable

[a]*Shenzhen Key Laboratory of Smart Healthcare Engineering, Guangdong Provincial Key Laboratory of Advanced Biomaterials, Department of Biomedical Engineering, Southern University of Science and Technology, No. 1088 Xueyuan Rd, Nanshan District, Shenzhen, Guangdong 518055, P. R. China. E-mail: jiang@sustech.edu.cn*

[b]*Institute for Advanced Study, Shenzhen University, No. 3688 Nanhai Avenue, Nanshan District, Shenzhen, Guangdong 518060, P. R. China*

† Electronic supplementary information (ESI) available: Experimental details and procedures, Fig. S1–S24, and Tables S1–S3. See DOI: https://doi.org/10.1039/d3sc02290k

‡ These authors contributed equally to this work.

for continuous visualization of dynamic physical processes. Recently, organic/inorganic nanohybrids have attracted tremendous attention by integrating the advantages of both organic and inorganic species;[33–35] and polyethylene glycol (PEG) functionalization is the current gold standard to shield protein adsorption and prolong blood circulation.[36–38] Constructing AuNP-based hybrid nanostructures with PEG functionalization may open a feasible pathway to enhance their NIR-II luminescence and optimize their *in vivo* biological behaviour. Nevertheless, the construction of AuNP-based organic/inorganic nanohybrids (AuNHs) with bright NIR-II emission and long blood circulation has yet to be discovered. The major obstacles lie in (a) the stabilization of ultrasmall AuNPs without aggregation during the preparation and maintenance of high emission in an aqueous medium; (b) the selection of applicable organic species to form the PEG layer on the surface, and regulation of the surface chemistry and formed morphology of AuNHs to be favourable for long blood circulation.

Herein, we present a one-pot fabrication of the AuNHs with bright NIR-II luminescence and controllable structure in a tunable manner for dynamic visualization of vascular dysfunction using amphiphilic block copolymer-assisted self-assembly (Scheme 1). This one-pot strategy was easy to reproduce and was excellent at overcoming luminescence quenching during the assembly. We selected the organic species Pluronic F127 as the template, and the template Pluronic F127 guided ultrasmall AuNP growth and assembly in the inner core and endowed them with PEG chains on the surface.[39,40] Two types of AuNHs with different assembled shapes and distinct surface PEG densities, including necklace-like AuNHs with a dense brush PEG coating and spherical AuNHs with a brush PEG surface, were obtained by changing the hydrophobic multidentate thiol ligands. Both AuNHs exhibited superior photostability, excellent deep tissue penetration, and good biosafety, but compared with the spherical AuNHs, the dense brush PEG surface enabled necklace-like AuNHs to show a higher QY in the NIR-II window, more effective shielding against protein adsorption and longer blood circulation. This one-pot fabrication approach effectively achieved bright NIR-II luminescence and long blood circulation properties simultaneously. As a proof of concept, the necklace-like AuNHs were utilized as an excellent nanoprobe for real-time imaging of the thrombolysis process. The real-time visualization of thrombolysis was a novel application for luminescent AuNPs, and these excellent performances might prompt more downstream applications of luminescent AuNPs.

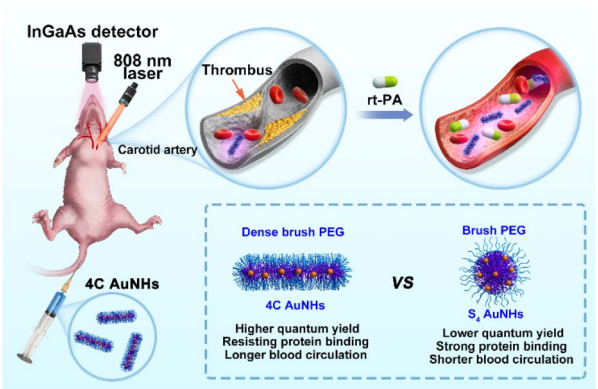

Scheme 1 Schematic illustration of the dynamic NIR-II imaging of vascular dysfunction and thrombolysis process. The inset shows the pros and cons of the 4C AuNHs and S_4 AuNHs.

Results and discussion

In a typical preparation, the hydrophobic thiol ligands and $HAuCl_4$ were successively located in the inner core of the template Pluronic F127 through the strong hydrophobic interaction and Au–S coordination, and subsequent reduction of metal precursors by $NaBH_4$ produced several ultrasmall AuNPs in the inner core of the template. Two kinds of multi-dentate thiol ligands, namely 1,4-butanedithiol (4C) and pentaerythritol tetrakis 3-mercaptopropionate (S_4), were employed for the preparation process of the AuNHs, respectively. Due to the different cross-linking abilities of the thiol ligands, the obtained AuNHs displayed different assembled shapes and distinct surface PEG coverage. In the synthetic process of 4C AuNHs, the template Pluronic F127 micelle remained a spherical structure with a hydrodynamic diameter (HD) of ~18 nm until the dialysis process (Fig. S1†). After dialysis against water, the HD was reduced to 8 nm, and a structural deformation occurred in the template micelle due to the limited cross-linking ability of 4C. From UV-vis absorption spectra (Fig. S2†), the Pluronic F127 micelle containing the 4C ligand showed no apparent absorbance in the 250–850 nm range. After adding $AuCl_4^-$, a broad absorption band around 340 nm appeared, suggesting the formation of Au(I)-thiolate. Then, after adding the reductant $NaBH_4$, the absorbance of the broad absorption band in the range of 250–850 nm gradually increased until the reaction ended at 3 h, suggesting the production of ultrasmall AuNPs in the Pluronic F127 micelle. Transmission electron microscopy (TEM) image showed that 4C-stabilized AuNHs (4C AuNHs) presented necklace-shaped nanostructures with a length size (L) of 36.1 ± 6.1 nm consisting of about 6 ultrasmall AuNPs with a core size of 1.88 ± 0.37 nm. The cryogenic transmission electron microscopy (cryo-TEM) image, which is a powerful tool for the characterization of colloidal polymer systems,[41] shows the linear structure of 4C AuNHs (width (W): 5.4 ± 1.0 nm) (Fig. 1a, c and Table 1). In contrast, S_4-stabilized AuNHs (S_4 AuNHs) were also composed of a similar number of ultrasmall AuNPs with a core size of 1.38 ± 0.30 nm. However, they were assembled into a spherical shape, and the cryo-TEM image also shows a spherical structure with a size of 13.0 ± 2.5 nm (D) (Fig. 1b, d and Table 1). The atomic force microscopy (AFM) images also indicated the necklace-shaped nanostructures of 4C AuNHs and the spherical shape of S_4 AuNHs (Fig. S3†). The assembled structure's tunability was closely related to the thiol ligands' cross-linking ability. As the carbon chain skeleton of bidentate thiol ligands gradually became longer, the spherical ratio in the assembled nanostructures increased from 8.5% for 4C AuNHs to 45.4% for 1,5-pentanedithiol (5C) stabilized AuNHs, to 86.2% for 1,8-

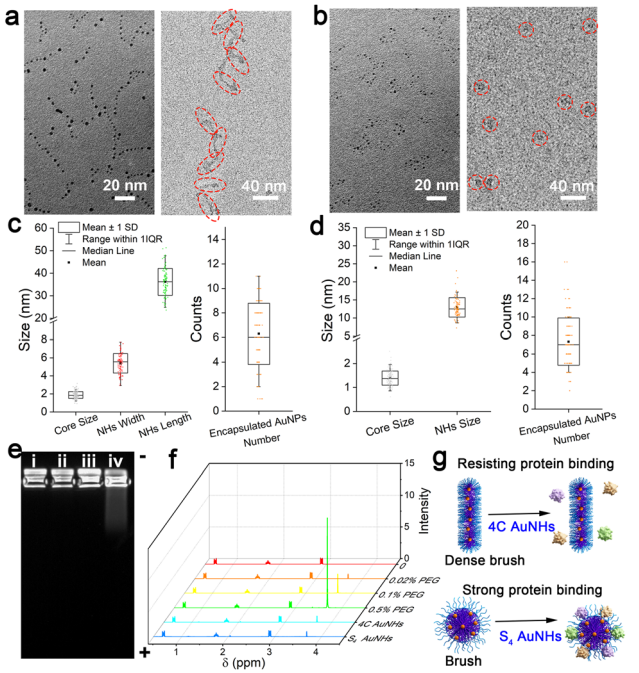

Fig. 1 Structural characterization of the AuNHs. TEM and cryo-TEM images of the 4C AuNHs (a) and S_4 AuNHs (b). The size distribution of the AuNP core, nanohybrids (left), and the number distribution of encapsulated AuNPs in an assembly (right) of the 4C AuNHs (c) and S_4 AuNHs (d). (e) Agarose gel electrophoresis of the AuNHs after incubation with 10% FBS. E_x (808 nm), E_m (1100 nm LP); (i) 4C AuNHs, (ii) 4C AuNHs + 10% FBS, (iii) S_4 AuNHs, (iv) S_4 AuNHs + 10% FBS. (f) ^{1}H NMR spectra of a series of PEG contents and the AuNHs in D_2O with 1 wt% 3-(trimethylsilyl)-1-propanesulfonic acid, sodium salt. (g) Schematic illustration of the AuNHs after incubation with 10% FBS.

octanedithiol (8C) stabilized AuNHs, suggesting that the cross-linking interaction was gradually enhanced as the bidentate thiol ligands lengthened, and the assembled shape tended to be spherical (Fig. S4 and S5†). To deeply understand their detailed structure, X-ray photoelectron spectroscopy (XPS) was used. A prominent peak (C–O bonds, 286.3 eV) appeared along with a weak or no signal for Au element in XPS spectra, indicating that a PEG layer derived from the Pluronic F127 template was covered on the surface of the AuNHs and no ultrasmall Au NPs were formed outside the PEG layer. After being gently treated with Ar^+ sputtering for the in-depth XPS analysis[40] (Fig. S6 and S7†), a dramatic reduction in C–O bonds and an increase in Au signal and C–C bonds suggested that ultrasmall AuNPs were formed within the hydrophobic inner core. These results illustrated that the two AuNHs shared similar Au core–PEG shell nanostructures. The contact angle of the two AuNHs was measured to be about 49° (Fig. S8†), illustrating that the two AuNHs exhibited outstanding water-solubility due to the PEG chains on their surface. The high-angle annular dark-field scanning transmission electron microscopy (HAADF-STEM) and elemental mapping experiments (Fig. S9 and S10†) revealed that the hydrophobic thiol ligands surrounded the ultrasmall AuNPs. These observations fully indicated that AuNHs with structural tunability and surface PEGylation could be achieved.

The shielding ability against protein adsorption was then studied by agarose gel electrophoresis, which was critical for prolonging blood circulation. The band of the 4C AuNHs did not migrate after incubation with 10% fetal bovine serum (FBS) in contrast to a noticeable shift in the S_4 AuNHs (Fig. 1e), indicating that the 4C AuNHs highly resisted protein adsorption, while the S_4 AuNHs adsorbed protein. The PEG density on the AuNH surface was characterized using an ^{1}H NMR method[42] and inductively coupled plasma mass spectrometry (ICP-MS) to reveal the different shielding abilities. The former was used to determine the surface PEG content, while the latter was applied to measure the concentrations of the AuNHs in combination with the TEM and cryo-TEM results. As shown in Fig. 1f, the PEG chains had a sharp peak at 3.65 ppm, and the peak area could be used to quantitatively determine the surface PEG content with a standard curve (Fig. S11†). Based on the concentration and the surface area of the AuNHs (equations are shown in the ESI†), the PEG density was calculated to be 15.1 ± 6.6 and 8.0 ± 3.2 PEG/100 nm^2 for the 4C AuNHs and S_4 AuNHs, respectively. These results indicated that the PEG chains of 4C AuNHs were in the dense brush configuration, while the PEG chains of S_4 AuNHs were in the brush configuration according to the ratio $[\Gamma]/[\Gamma^*]$ results (Table 1), which reflected the packed PEG configuration ($[\Gamma]/[\Gamma^*] < 1$: mushroom configuration; $1 < [\Gamma]/[\Gamma^*] < 2$: brush configuration; $[\Gamma]/[\Gamma^*] > 2$: dense brush configuration).[42,43] The different PEG configurations could be attributed to the different cross-linking abilities of the thiol ligands: S_4 had a powerful cross-linking ability and could enable the template Pluronic F127 to retain the spherical structure with the brush configuration; in contrast, 4C had less cross-linking ability and the template became deformed, rearranged, and reassembled into the linear structure with the dense brush configuration due to depletion interactions during dialysis against water.[44,45] Due to the different PEG configurations formed on the surface, the two AuNHs presented distinct shielding abilities against protein adsorption (Fig. 1g).

As shown in Fig. 2a, the two AuNHs displayed a broad absorbance in the range of 300–850 nm, and no surface plasmonic resonance absorbance at 520 nm assigned to large AuNPs was observed. The maximum emission peak was located

Table 1 Physicochemical characterization and calculated PEG density of the AuNHs

	Core size (nm)	NH size (nm)	Encapsulated NP number	PEG density/(PEG/100 nm^2)	$[\Gamma]/[\Gamma^*]$	PEG configuration
4C AuNHs	1.88 ± 0.37	5.4 ± 1.0 (*W*); 36.1 ± 6.1 (*L*)	6.25 ± 2.53	15.1 ± 6.6	3.0 ± 1.3	Dense brush
S_4 AuNHs	1.38 ± 0.30	13.0 ± 2.5 (*D*)	7.32 ± 2.59	8.0 ± 3.2	1.6 ± 0.6	Brush

at 1070 nm under 808 nm excitation. Using different long-pass (LP) filters, both AuNHs presented bright luminescence (Fig. S12†). The QYs were measured to be 0.59% and 0.11% for the 4C AuNHs and the S_4 AuNHs using IR-1061 as the reference (QY = 0.59% in dichloromethane).[46,47] The QY of the 4C AuNHs was superior to that of most of the previously reported water-soluble AuNPs and NIR-II emitting organic dyes (Table S1†). The enhanced luminescence of the 4C AuNHs was attributed to an efficient bridge among ultrasmall AuNPs with an appropriate amount of Au(I) species (23.02%) and effective protection by the dense surface PEG in the brush configuration,[48] while the lower QY of the S_4 AuNHs was ascribed to the nonradiative decay enhancement due to the smaller amount of Au(I) species (7.4%) and lower surface PEG coverage. The luminescence decay experiments (Fig. 2b and Table S2†) showed that the average lifetime of the S_4 AuNHs (2.00 μs) was shorter than that of the 4C AuNHs (2.90 μs), further confirming the nonradiative decay enhancement of the S_4 AuNHs. The thiol ligands 4C and Pluronic F127 were essential in the assembled necklace-like shape and NIR-II emission (Fig. S13–S16†). The luminescence of the two AuNHs exhibited good stability in different media, such as water, PBS, Dulbecco's Modified Eagle Medium (DMEM), and DMEM supplemented with 10% FBS, and no noticeable decrease in their luminescence intensities was observed even after being stored for 7 days at room temperature (Fig. 2c and S17†). Moreover, the two types of AuNHs also showed superior photostability on exposing them to continuous 808 nm laser irradiation for 150 min (Fig. 2d, S18 and S19†). When the capillary tubes loading 4C AuNHs, S_4 AuNHs, and indocyanine green (ICG) solution submerged in 1% Intralipid solution with different depths, respectively, 4C AuNHs and S_4 AuNHs presented a coherent picture even at a 6 mm depth, confirming that the two types of AuNHs had an excellent deep tissue penetration (Fig. 2e and f). These results demonstrated that the AuNHs were a promising NIR-II contrast agent and had potential in downstream biological imaging.

Biological safety is of great significance to further *in vivo* applications. As indicated in Fig. 3a, hemolysis tests demonstrated that the two types of AuNHs did not induce erythrocyte lysis even at a high concentration of 400 μg ml^{-1}. Cell viability analysis was conducted on human umbilical vein endothelial cells (HUVECs) using a calcein AM and propidium iodide (PI) protocol and CCK-8 assays, and no noticeable decrease in the cell viability and no obvious dead cells were observed when treated with a concentration of 40 μg ml^{-1} for 24 h (Fig. 3b and S20†), suggesting that both AuNHs exhibited negligible cytotoxicity. To further estimate their *in vivo* bio-safety, the two types of AuNHs were administered to mice through tail intravenous (i.v.) injection at an applied concentration at 7 days post injection (p.i.). The major organs, including the heart, liver, spleen, lung, and kidney, were stained by hematoxylin and eosin (H&E) staining for histological analysis (Fig. S21†). H&E staining showed no obvious inflammation and trauma in the major organs for all experimental groups. Moreover, as shown

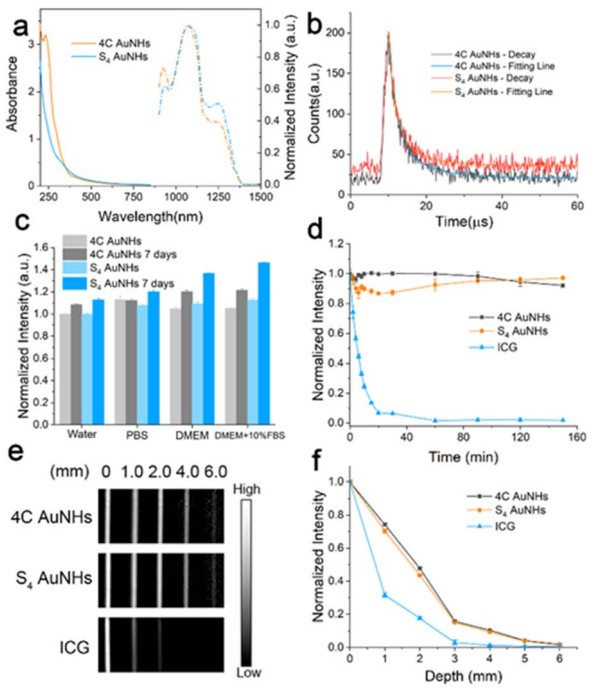

Fig. 2 Optical characterization of the 4C AuNHs and S_4 AuNHs. (a) Absorption and emission spectra of the 4C AuNHs and S_4 AuNHs. (b) Time-resolved decay of the 4C AuNHs and S_4 AuNHs. (c) Stability of the 4C AuNHs and S_4 AuNHs in different media after storage for 7 days at room temperature. (d) Photostability of the 4C AuNHs, S_4 AuNHs, and ICG in water under continuous 808 nm laser irradiation for 150 min with a power density of 0.33 W cm^{-2}. NIR images (e) and normalized intensity (f) of the 4C AuNHs (top, λ_{ex} = 808 nm, 1100 nm LP), S_4 AuNHs (middle, λ_{ex} = 808 nm, 1100 nm LP), and ICG (bottom, λ_{ex} = 780 nm, 830 nm LP) submerged in 1% Intralipid solution with different depths.

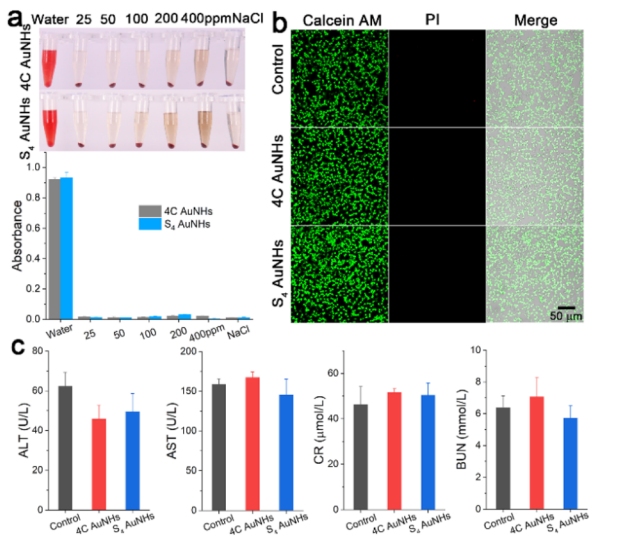

Fig. 3 Biological safety of the 4C AuNHs and S_4 AuNHs. (a) Hemolysis of the 4C AuNHs and S_4 AuNHs with different concentrations against fresh erythrocytes. (b) Confocal images of HUVEC without or with the treatment of 40 μg ml^{-1} 4C AuNHs and S_4 AuNHs stained with calcein AM (a dye for living cells) and PI (a dye for dead cells). (c) Biochemical index analysis for liver function and kidney function after the treatment of 4C AuNHs and S_4 AuNHs at 7 days p.i.

in Fig. 3c and S22,† a series of biochemical blood indexes after the treatment of 4C AuNHs and S_4 AuNHs at 7 days p.i., including alanine transaminase (ALT), aspartate transaminase (AST), creatinine (CR), blood urea nitrogen (BUN), white blood cells (WBCs), red blood cells (RBCs) and platelets (PLT), were all located in the normal levels, indicating the excellent biocompatibility of these AuNHs. The excellent biosafety could prompt the AuNHs to be an ideal candidate for *in vivo* imaging.

The NIR-II emission could endow these AuNHs with deep tissue penetration ability and high imaging resolution, offering a powerful pathway for determining their *in vivo* biological behaviour. To investigate the effect of structural difference on pharmacokinetics, the NIR-II imaging of mice brains was conducted at different time points p.i. of the AuNHs (5 mg kg^{-1}). The brain vessel could be visualized with 4C AuNH administration; small vessels were still legibly visible even at 3 h p.i. (Fig. 4a). In contrast, no clear signal from the brain vessel was observed for S_4 AuNHs at 0.5 h p.i. and ICG at 5 min p.i. (Fig. 4a and S23†), and the S_4 AuNHs with a brush PEG surface and ICG were rapidly eliminated from the blood. To reveal the spatial resolving ability of the 4C AuNHs, the vessel imaging of mice brain was performed using a 1300 nm long-pass (LP) filter (Fig. 4b), and the signal-to-background ratio (SBR) value could reach 4.99. To reveal the pharmacokinetics difference between 4C AuNHs and S_4 AuNHs, the Au content in the blood samples at different time points p.i. was monitored using ICP-MS. As shown in Fig. 4c, the mice with 4C AuNH administration could still maintain a high blood Au content of 20.67% ID per g at 3 h p.i. The blood Au content with S_4 AuNH administration fell to a baseline level. The blood half-life of 4C AuNHs (3.44 h) and areas under the curves (AUCs, 301.66% ID h per g) were much higher than those of S_4 AuNHs (10 min, 114.52% ID h per g) and were also superior to the previously reported AuNPs (Table S3†). The *ex vivo* images of blood at 1 h post i.v. injection (Fig. 4c inset) showed that the blood with 4C AuNHs emitted a significantly brighter signal than the blood with S_4 AuNHs. These results unambiguously proved that the necklace-like 4C AuNHs showed longer blood retention than spherical S_4 AuNHs, although they had surface PEGylation. The biodistribution results further revealed that the 4C AuNHs remained in the blood and were less distributed in the organs. At the same time, most S_4 AuNHs were rapidly eliminated from blood and captured by the liver and spleen due to the strong binding with serum proteins and clearance by the reticuloendothelial system (Fig. 1e, 4d and e).[36–38] Compared with the bioaccumulation at 1 h p.i., no noticeable change occurred in the bioaccumulation of S_4 AuNHs, while the 4C AuNHs were eliminated from blood during this time and captured by the liver and spleen, resulting in the accumulation of the 4C AuNHs, which increased from 6.2% ID per g in the liver and 4.6% ID per g in the spleen at 1 h p.i. to 39.7% ID per g in the liver and 16.6% ID per g in the spleen at 24 h p.i. (Fig. S24†). The above observations fully indicated that the necklace-like 4C AuNHs with a dense brush PEG configuration possessed bright emission, superior photostability, excellent deep tissue penetration, good biosafety, and prolonged blood retention, and could be appropriate for long-term blood vessel imaging.

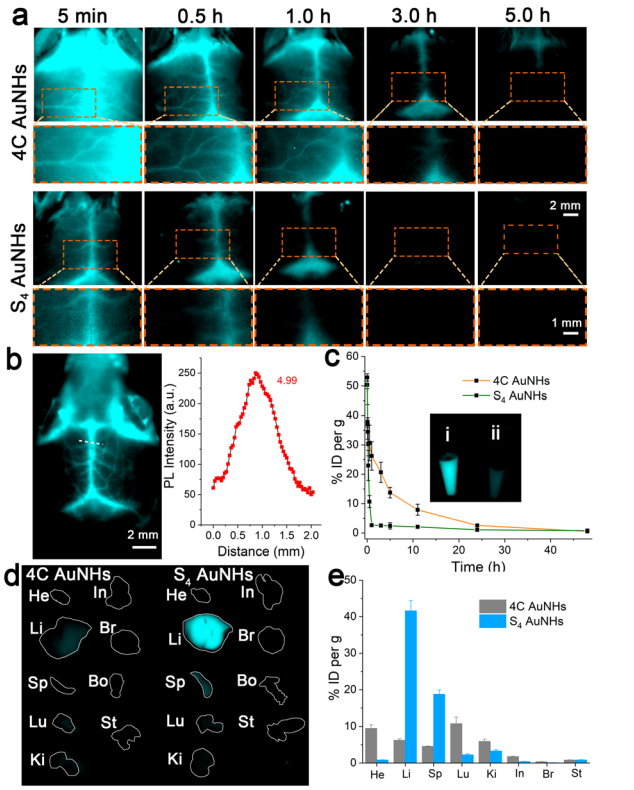

Fig. 4 Pharmacokinetics and biological distribution of the 4C AuNHs and S_4 AuNHs. (a) NIR-II imaging of mice brain after i.v. injection with the AuNHs (5 mg kg^{-1}) at different time points (0.145 W cm^{-2}, 1100 nm LP, λ_{ex} = 808 nm, 800 ms), orange dashed boxes show the partially enlarged images. (b) NIR image of the brain after i.v. injection with the 4C AuNHs (0.145 W cm^{-2}, 1300 nm LP, λ_{ex} = 808 nm, 2000 ms), the luminescence intensity profile along the white line in the brain. (c) Pharmacokinetics of the 4C AuNHs and S_4 AuNHs after i.v. injection (n = 3). The inset showed the *ex vivo* images of blood at 1 h post i.v. injection of the 4C AuNHs (i) and S_4 AuNHs (ii). The *ex vivo* images (d) and bioconcentration (e) of main organs and tissues were collected at 1 h post i.v. injection of the 4C AuNHs and S_4 AuNHs. He: heart, Li: liver, Sp: spleen, Lu: lung, Ki: kidney, In: intestine, Br: brain, Bo: bone, St: stomach.

Thrombosis, a clot inside a blood vessel, is closely associated with many life-threatening cardiovascular diseases,[49] and real-time and sustaining visualization of thrombolysis is critical to the clinical translation of therapeutic drugs. To estimate the imaging effectiveness during the thrombolysis process, recombinant tissue plasminogen activator (rt-PA), widely utilized as a clinical medicine to treat the thrombosis,[50] is employed as a representative medicine for the breakdown of the blood clot. The $FeCl_3$-induced vascular injury method was introduced to establish the mouse thrombosis model on the right carotid artery.[51] As illustrated in Fig. 5a and Scheme 1, 4C AuNHs were i.v. injected first to brighten the carotid artery and direct the thrombus location, and then real-time NIR-II imaging of the carotid artery was performed along with the i.v. injection of rt-PA with different doses. The H&E staining showed the formation of a thrombus on the right carotid artery (Fig. 5a). Since the thrombus could block blood flow, NIR-II imaging observed a thrombus shadow. Initially, a low dose of rt-PA (100 μl, 0.015 mg ml^{-1}) was i.v. injected into the

mouse, but no apparent change occurred in the thrombus shadow, even at 8.30 min (ESI Movie 1†). Then, rt-PA administration increased to a high dose (100 μl, 0.15 mg ml^{-1}), and the thrombus shadow started to dissolve at 2.73 min and rapidly disappeared at 2.74 min. The NIR-II signals of the carotid artery continuously increased, and the complete blood vessel was present clearly in the following time, suggesting that the carotid artery showed patency after the breakdown of the thrombus (Fig. 5b, ESI Movie 2†). The increase in background signals might be related to high doses of rt-PA. When the wound produced during the $FeCl_3$-induced vascular injury process was exposed to the high dose of rt-PA, some probes would spill and accumulate in the imaging view along with ruptured small vessels. It should be noted that the left carotid artery showed a clear visualization without decreasing the signal during the thrombolysis process, indicating the long blood circulation and excellent imaging capability of the 4C AuNHs. The above observations illustrated that 4C AuNHs could be an excellent NIR-II probe for real-time, dynamic visualization of vascular dysfunction and directing the precise administration of thrombolytics.

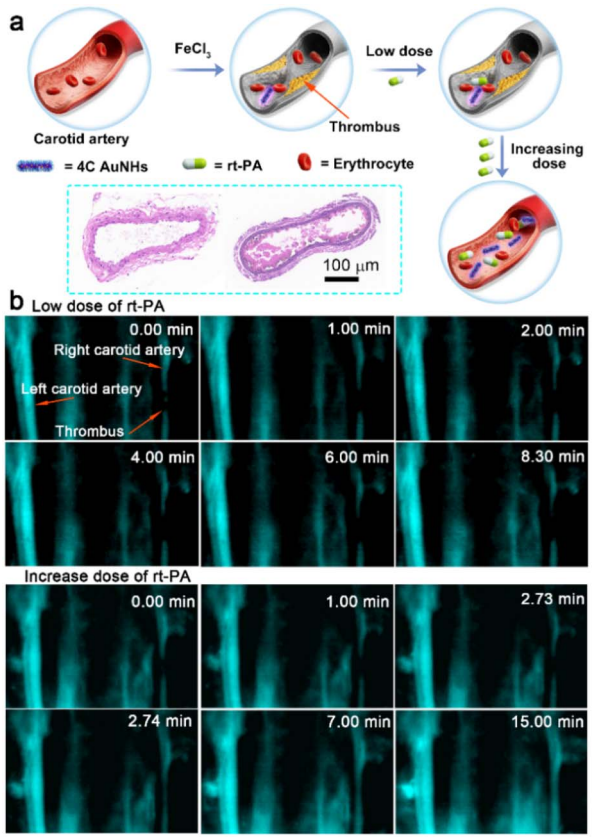

Fig. 5 Dynamic NIR-II imaging of mouse carotid artery during the thrombolysis process. (a) Schematic illustration of $FeCl_3$-induced vascular injury and the thrombolysis process. The dashed box showed H&E staining of the carotid artery without (left) or with (right) $FeCl_3$ treatment. (b) NIR-II imaging of the carotid arteries at various time points p.i. of a low dose of rt-PA (top, 100 μl, 0.015 mg ml^{-1}) and subsequent increasing dose of rt-PA (down, 100 μl, 0.15 mg ml^{-1}) administration after i.v. injection of the 4C AuNHs (0.145 W cm^{-2},1100 nm LP, λ_{ex} = 808 nm, 250 ms).

Conclusions

In summary, we reported a one-pot synthetic protocol for NIR-II emitting AuNHs in a controlled manner as an efficient contrast agent for imaging vascular dysfunction. The template Pluronic F127 directed ultrasmall AuNPs to assemble in the inner core and keep their surfaces PEGylated. By varying the hydrophobic thiol ligands, the nanostructures could be controlled from a sphere with a brush PEG configuration to a necklace-like shape with a dense brush PEG configuration by controlling the cross-linking interaction among ultrasmall AuNPs. The AuNHs possessed bright NIR-II emission, superior photostability, excellent deep tissue penetration, and good biosafety. Due to the dense brush PEG configuration on the surface, the necklace-like AuNHs displayed much higher QY and longer blood retention than the spherical AuNHs. Because of these outstanding features, the necklace-like AuNHs could achieve real-time, dynamic visualization of vascular dysfunction and direct the precise administration of thrombolytics. These findings offered a useful guide for the rational design and efficient fabrication of a novel NIR-II AuNP-based nanoprobe in a tunable and controllable manner to prolong blood circulation and direct precise drug administration. NIR-II luminescence could overcome the penetration/contrast bottleneck of imaging in the visible region and probe tissue at a depth of 1.5 cm.[52] Since the vertical distance from the skin to the anterior adventitia of the carotid was about 1.0 cm,[53] this protocol might have great promise in the early diagnosis of thrombus and in directing the precise administration of thrombolytics. In the future, this one-pot synthesis, with the help of microfluidics and laser ablation, could achieve the design of uniform nanomaterials with precisely assembled morphology and exact PEG surface coverage. The strategy could also be adjusted for loading various drugs to explore new potential applications, such as cancer therapies and antibacterial drugs and scaffold materials for tissue engineering.

Ethical statement

All animal experiments were performed in compliance with the relevant laws and institutional guidelines. All procedures for animal studies were conducted according to the approved protocols by the Institutional Animal Care and Use Committee of the Southern University of Science and Technology (SUSTech-JY2020103058). Informed consent was obtained for any experimentation with human subjects.

Data availability

All experimental supporting data and procedures associated with this article have been provided in the ESI.†

Author contributions

T. Z. and X. J. conceived the study; T. Z. and M. Z. performed the experiments and analysed the data; H. T. and K. L. helped with the data collection; T. Z. and X. J. wrote and revised the

manuscript; all authors discussed the results and approved the final version of the manuscript.

Conflicts of interest

There are no conflicts to declare.

Acknowledgements

We acknowledge the financial support from the National Key Research and Development Program of China (No. 2021YFF1200100, 2018YFA0902600, 2020YFA0908900, 2021YFF1200800), the National Natural Science Foundation of China (No. 21907032, 81730051, 22234004, 32071390), Shenzhen Science and Technology Program (No. KQTD20190929172743294, JCYJ20200109141231365), Guangdong Provincial Key Laboratory of Advanced Biomaterials (No. 2022B1212010003), Shenzhen Key Laboratory of Smart Healthcare Engineering (No. ZDSYS20200811144003009), Guangdong Innovative and Entrepreneurial Research Team Program (No. 2019ZT08Y191), Guangdong Major Talent Introduction Project (No. 2019CX01Y196) and Tencent Foundation through the XPLORER PRIZE. The authors acknowledge the assistance of SUSTech Core Research Facilities and the Cryo-EM facility of Southern University of Science and Technology for providing the facility support.

Notes and references

1 V. L. Feigin, M. H. Forouzanfar, R. Krishnamurthi, G. A. Mensah, M. Connor, D. A. Bennett, A. E. Moran, R. L. Sacco, L. Anderson, T. Truelsen, M. O'Donnell, N. Venketasubramanian, S. Barker-Collo, C. M. Lawes, W. Wang, Y. Shinohara, E. Witt, M. Ezzati, M. Naghavi and C. Murray, *Lancet*, 2014, **383**, 245–254.

2 G. Pasterkamp, H. M. den Ruijter and P. Libby, *Nat. Rev. Cardiol.*, 2017, **14**, 21–29.

3 S. Cheng, C. Hang, L. Ding, L. Jia, L. Tang, L. Mou, J. Qi, R. Dong, W. Zheng, Y. Zhang and X. Jiang, *Matter*, 2020, **3**, 1664–1684.

4 J. W. Goldfarb and J. Weber, *Radiol.: Cardiothorac. Imaging*, 2021, **3**, e200112.

5 K. Nishimiya, Y. Matsumoto and H. Shimokawa, *Arterioscler. Thromb. Vasc. Biol.*, 2020, **40**, e313–e321.

6 X. Zhao, F. Zhang and Z. Lei, *Chem. Sci.*, 2022, **13**, 11280–11293.

7 C. Li, G. Chen, Y. Zhang, F. Wu and Q. Wang, *J. Am. Chem. Soc.*, 2020, **142**, 14789–14804.

8 G. Hong, A. L. Antaris and H. Dai, *Nat. Biomed. Eng.*, 2017, **1**, 0010.

9 G. Hong, S. Diao, J. Chang, A. L. Antaris, C. Chen, B. Zhang, S. Zhao, D. N. Atochin, P. L. Huang, K. I. Andreasson, C. J. Kuo and H. Dai, *Nat. Photonics*, 2014, **8**, 723–730.

10 Z. Ma, M. Zhang, J. Yue, C. Alcazar, Y. Zhong, T. C. Doyle, H. Dai and N. F. Huang, *Adv. Funct. Mater.*, 2018, **28**, 1803417.

11 H. D. A. Santos, I. Z. Gutierrez, Y. L. Shen, J. Lifante, E. Ximendes, M. Laurenti, D. Mendez-Gonzalez, S. Melle, O. G. Calderon, E. L. Cabarcos, N. Fernandez, I. Chaves-Coira, D. Lucena-Agell, L. Monge, M. D. Mackenzie, J. Marques-Hueso, C. M. S. Jones, C. Jacinto, B. del Rosal, A. K. Kar, J. Rubio-Retama and D. Jaque, *Nat. Commun.*, 2020, **11**, 2933.

12 C. Sun, B. Li, M. Zhao, S. Wang, Z. Lei, L. Lu, H. Zhang, L. Feng, C. Dou, D. Yin, H. Xu, Y. Cheng and F. Zhang, *J. Am. Chem. Soc.*, 2019, **141**, 19221–19225.

13 B. Li, M. Zhao, L. Feng, C. Dou, S. Ding, G. Zhou, L. Lu, H. Zhang, F. Chen, X. Li, G. Li, S. Zhao, C. Jiang, Y. Wang, D. Zhao, Y. Cheng and F. Zhang, *Nat. Commun.*, 2020, **11**, 3102.

14 Y. Li, Z. Cai, S. Liu, H. Zhang, S. T. H. Wong, J. W. Y. Lam, R. T. K. Kwok, J. Qian and B. Z. Tang, *Nat. Commun.*, 2020, **11**, 1255.

15 Z. Cai, L. Zhu, M. Wang, A. W. Roe, W. Xi and J. Qian, *Theranostics*, 2020, **10**, 4265–4276.

16 S. He, S. Chen, D. Li, Y. Wu, X. Zhang, J. Liu, J. Song, L. Liu, J. Qu and Z. Cheng, *Nano Lett.*, 2019, **19**, 2985–2992.

17 H. Li, X. Wang, X. Li, S. Zeng and G. Chen, *Chem. Mater.*, 2020, **32**, 3365–3375.

18 Z. Zhang, X. F. Fang, Z. H. Liu, H. C. Liu, D. D. Chen, S. Q. He, J. Zheng, B. Yang, W. P. Qin, X. J. Zhang and C. F. Wu, *Angew. Chem., Int. Ed.*, 2020, **59**, 3691–3698.

19 K. Zheng and J. Xie, *Trends Chem.*, 2020, **2**, 665–679.

20 Y. Zheng, J. Wu, H. Jiang and X. Wang, *Coord. Chem. Rev.*, 2021, **431**, 213689.

21 G. Yang, X. Mu, X. Pan, Y. Tang, Q. Yao, Y. Wang, F. Jiang, F. Du, J. Xie, X. Zhou and X. Yuan, *Chem. Sci.*, 2023, **14**, 4308–4318.

22 J. Zhang, L. Mou and X. Jiang, *Chem. Sci.*, 2020, **11**, 923–936.

23 L. Wang, S. Li, J. Yin, J. Yang, Q. Li, W. Zheng, S. Liu and X. Jiang, *Nano Lett.*, 2020, **20**, 5036–5042.

24 H. Ma, J. Wang and X. D. Zhang, *Coord. Chem. Rev.*, 2021, **448**, 214184.

25 S. Li, Q. Ma, C. Wang, K. Yang, Z. Hong, Q. Chen, J. Song, X. Song and H. Yang, *Anal. Chem.*, 2022, **94**, 2641–2647.

26 D. Li, Q. Liu, Q. Qi, H. Shi, E. C. Hsu, W. Chen, W. Yuan, Y. Wu, S. Lin, Y. Zeng, Z. Xiao, L. Xu, Y. Zhang, T. Stoyanova, W. Jia and Z. Cheng, *Small*, 2020, **16**, e2003851.

27 H. Liu, G. Hong, Z. Luo, J. Chen, J. Chang, M. Gong, H. He, J. Yang, X. Yuan, L. Li, X. Mu, J. Wang, W. Mi, J. Luo, J. Xie and X. D. Zhang, *Adv. Mater.*, 2019, **31**, e1901015.

28 W. L. Wang, Y. F. Kong, J. Jiang, Q. Q. Xie, Y. Huang, G. N. Li, D. Wu, H. Z. Zheng, M. Gao, S. J. Xu, Y. X. Pan, W. Li, R. L. Ma, M. X. Wu, X. H. Li, H. Zuilhof, X. M. Cai and R. B. Li, *Angew. Chem., Int. Ed.*, 2020, **59**, 22431–22435.

29 Z. Pang, Q. Li, Y. Jia, W. Yan, J. Qi, Y. Guo, F. Hu, D. Zhou and X. Jiang, *Chem. Sci.*, 2021, **12**, 14871–14882.

30 Z. Yu, B. Musnier, K. D. Wegner, M. Henry, B. Chovelon, A. Desroches-Castan, A. Fertin, U. Resch-Genger, S. Bailly, J.-L. Coll, Y. Usson, V. Josserand and X. Le Guével, *ACS Nano*, 2020, **14**, 4973–4981.

31 Y. Yang, Y. Yu, H. Chen, X. Meng, W. Ma, M. Yu, Z. Li, C. Li, H. Liu, X. Zhang, H. Xiao and Z. Yu, *ACS Nano*, 2020, **14**, 13536–13547.
32 A. Baghdasaryan, F. Wang, F. Ren, Z. Ma, J. Li, X. Zhou, L. Grigoryan, C. Xu and H. Dai, *Nat. Commun.*, 2022, **13**, 5613.
33 W. Chen, C. A. Cheng, E. D. Cosco, S. Ramakrishnan, J. G. P. Lingg, O. T. Bruns, J. I. Zink and E. M. Sletten, *J. Am. Chem. Soc.*, 2019, **141**, 12475–12480.
34 P. Pei, H. Hu, Y. Chen, S. Wang, J. Chen, J. Ming, Y. Yang, C. Sun, S. Zhao and F. Zhang, *Nano Lett.*, 2022, **22**, 783–791.
35 B. Li, M. Zhao, J. Lin, P. Huang and X. Chen, *Chem. Soc. Rev.*, 2022, **51**, 7692–7714.
36 H. Zhao, Y. Wang, L. Bao and C. Chen, *Acc. Mater. Res.*, 2022, **3**, 812–829.
37 J. L. Perry, K. G. Reuter, M. P. Kai, K. P. Herlihy, S. W. Jones, J. C. Luft, M. Napier, J. E. Bear and J. M. DeSimone, *Nano Lett.*, 2012, **12**, 5304–5310.
38 R. Cai and C. Chen, *Adv. Mater.*, 2019, **31**, e1805740.
39 T. Zhou, J. Zhu, L. Gong, L. Nong and J. Liu, *J. Am. Chem. Soc.*, 2019, **141**, 2852–2856.
40 H. L. Ma, T. Y. Zhou, Z. Y. Dai, J. Q. Hu and J. B. Liu, *Adv. Opt. Mater.*, 2019, **7**, 1900326.
41 J. J. Crassous, C. N. Rochette, A. Wittemann, M. Schrinner, M. Ballauff and M. Drechsler, *Langmuir*, 2009, **25**, 7862–7871.
42 Q. Xu, L. M. Ensign, N. J. Boylan, A. Schön, X. Gong, J. C. Yang, N. W. Lamb, S. Cai, T. Yu, E. Freire and J. Hanes, *ACS Nano*, 2015, **9**, 9217–9227.
43 X. Jiang, D. A. Bruzewicz, M. M. Thant and G. M. Whitesides, *Anal. Chem.*, 2004, **76**, 6116–6121.
44 T. Zhou, Q. Li, Y. Chen and X. Jiang, *Chem. Commun.*, 2020, **56**, 14023–14026.
45 T. Zhou and X. Jiang, *Chem. Sci.*, 2022, **13**, 12107–12113.
46 R. Hoshi, K. Suzuki, N. Hasebe, T. Yoshihara and S. Tobita, *Anal. Chem.*, 2020, **92**, 607–611.
47 Z. Liu, Y. Li, E. Kahng, S. Xue, X. Du, S. Li and R. Jin, *ACS Nano*, 2022, **16**, 18448–18458.
48 M. A. H. Muhammed, F. Aldeek, G. Palui, L. Trapiella-Alfonso and H. Mattoussi, *ACS Nano*, 2012, **6**, 8950–8961.
49 N. Mackman, W. Bergmeier, G. A. Stouffer and J. I. Weitz, *Nat. Rev. Drug Discovery*, 2020, **19**, 333–352.
50 S. Y. Liu, W. F. Cao, L. F. Wu, Z. B. Xiang, S. M. Liu, H. Y. Liu, Y. Pan, F. Nie, X. M. Wu and X. F. Xie, *Medicine*, 2018, **97**, e13216.
51 T. Bonnard and C. E. Hagemeyer, *J. Vis. Exp.*, 2015, **100**, e52838.
52 A. L. Antaris, H. Chen, K. Cheng, Y. Sun, G. Hong, C. Qu, S. Diao, Z. Deng, X. Hu, B. Zhang, X. Zhang, O. K. Yaghi, Z. R. Alamparambil, X. Hong, Z. Cheng and H. Dai, *Nat. Mater.*, 2016, **15**, 235–242.
53 J. A. Gerstenhaber, F. C. Barone, C. Marcinkiewicz, J. Li, A. O. Shiloh, M. Sternberg, P. I. Lelkes and G. Feuerstein, *Int. J. Nanomedicine*, 2017, **12**, 8471–8482.